CHEMISTRY OF MATERIALS

ARTICLE

pubs.acs.org/cm

Mechanistic Studies on Sintering of Silver Nanoparticles

Steven K. Volkman,*,† Shong Yin,† Teymur Bakhishev,† Kanan Puntambekar,† and Vivek Subramanian†

†Department of Electrical Engineering and Computer Sciences, University of California, Berkeley, Berkeley, California 94720, United States

Michael F. Toney‡

‡Stanford Synchrotron Radiation Lightsource, Menlo Park, California 94025, United States

Supporting Information

ABSTRACT: Metal nanoparticles are known to form highly conductive films upon heating below 200 °C. We study the mechanism and morphological changes that occur as 3 nm, thiolate encapsulated, silver nanoparticles are annealed to form conductive films. We use X-ray diffraction (XRD), grazing incidence X-ray scattering (GIXS), and transmission electron microscopy (TEM) to monitor structural changes in the film. We show that the surfactant is present during the entire sintering process, that its presence greatly influences the grain size and crystallite orientation of the resulting film, and that the film becomes fully conductive in the presence of the surfactant. We show that particles that aggregate more rapidly form films that consist of smaller crystallites and are less textured. We further show that digestive ripening can lead to the degeneration of films back into particles, particularly when annealing in air versus an inert environment. Coalescence contributes to crystallite growth when particles are small but can confound both crystallite size and orientation development in the later stages of growth. The interaction of the surfactant with the particle is weakened by moisture, lowering the temperature at which the surfactant disassociates from the particle and sintering begins. Moisture also increases the rate of both aggregation and digestion, drastically changing the morphology of the films at any given temperature.

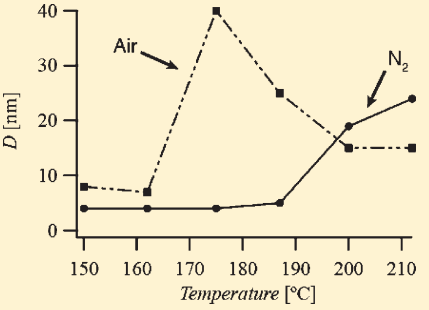

KEYWORDS: silver, inkjet printing, solution processing, thin film, sinter

1. INTRODUCTION

The physical properties of nanoparticles differ from those of their bulk counterparts, as a result of their reduced size and dimension.[1−3] Consequently, metal nanoparticles are under intense investigation with applications in catalysis,[4] photonics,[5−7] medicine,[8] and, of interest here, in sintered systems for low cost, large area electronics,[9−11] including photovoltaics.[12−14] Huang first described the sintering of solution deposited metal particles to form conductive films at plastic compatible temperatures.[15] Since then, the use of nanoparticles in printed electronics has been ubiquitous. Only a few studies have been reported on the sintering of monolayer-encapsulated nanoparticles into conductive films, and these tend to focus more on the application of these films in devices[16] or an a particular aspect of the sintering process.[17] This lack is surprising given the widespread use of sintered nanoparticles over the past decade and, indeed, represents a tremendous gap in our knowledge that should be filled to allow for proper understanding and optimized deployment of sintered nanoparticle films for electronic applications.

Broadly speaking, for printed electronics applications, interest lies in particles that can be suspended in a solution, applied to a substrate as a liquid, and then, through heating, or other input of energy, converted into a conductive thin film with conductivities orders of magnitude greater than the metal flake inks currently in production. This requires that the particles are nanometer sized, because larger particles flocculate, leading to difficulty in printing, and sinter at considerably higher temperatures, preventing plastic compatibility. However, the high surface energy of naked nanoparticles[18] leads to aggregation and thus flocculation; therefore, the surface of the particles must be passivated, which is often accomplished by coating the particles with a self-assembled monolayer (SAM). For printed films derived from metallic nanoparticles, a better understanding of the anneal process is needed to maximize conductivity in the resultant thin film and to allow tuning of the processing conditions to meet application and substrate imposed constraints.

Here, we study the sintering of thiol encapsulated silver nanoparticles, which are an important subclass of the more general surfactant pacified nanoparticles. We show that the surfactant is present during the entire sintering process, that its presence greatly influences the grain size and crystal orientation of the resulting film, and that the film becomes fully conductive in the presence of the surfactant.

Crystallite growth can occur by several different mechanisms, with aggregative growth[19] and Ostwald ripening[20] being the dominant mechanisms mentioned in the literature. In this study we examine the effect of aggregation on particle and film growth.

Received: August 26, 2011
Published: October 04, 2011

dx.doi.org/10.1021/cm202561u | Chem. Mater. 2011, 23, 4634–4640

Aggregative growth involves the aggregation of two or more particles to form a larger crystallite.[21,22] It is confirmed by the presence of characteristic oblong particles sharing a common crystallographic orientation or by the direct observation of aggregated nanoparticles at some earlier time and their disappearance at some later time. Aggregation of particles is characterized by the presence of polycrystallinity and twinning in particles. Coalescence contributes to crystallite growth in the early stage of the sintering process, but aggregation confounds the growth and orientation of films in later stages of growth. For the particles studied herein, the rate of aggregation is faster in air than in inert environments at the same temperature.

Digestive ripening is a process by which smaller particles grow as larger particles are eroded away. This mechanism is rather opposite of Ostwald ripening where larger particles are fed by the disappearance of higher surface energy, smaller particles. Digestive ripening can be seen from characteristic superlattices that form as larger particles are eroded.[23,24] It is not present in the early stages of sintering, when there are relatively smaller particles, and, for the system studied herein, is only observed in air anneals.

For applications in low-cost electronics focusing on plastic substrates, such as polyethylene naphthalate (PEN) and polyethylene terephthalate (PET), the substrate limits the annealing temperatures to around 200 °C for PEN or lower for PET, and so we limit our study to these temperatures. In 16 min at 200 °C, our films become conductive with a resistivity of 9×10^{-6} Ω-cm (17% of bulk silver conductivity), and hence we study the development of film morphology and its effect on electrical conductivity over this time frame. We employ differential scanning calorimetry (DSC) to monitor phase transitions and thermal gravimetric analysis (TGA) to monitor mass transport into and out of the material as it is heated. These provide an overview of the various thermodynamic transitions that occur as the nanoparticles are annealed and sinter into a film. This is then correlated to the nanoparticle structure to develop a mechanistic model of the nanoparticle sintering. Crystal orientation and grain size are determined using X-ray diffraction (XRD), the presence of a nanoparticle superlattice using grazing incidence X-ray scattering (GIXS), and particle size and morphology using transmission electron microscopy (TEM). From these results, we propose a comprehensive explanation of the processes occurring during sintering of thiol encapsulated silver nanoparticles. This is critical to the optimization of particles and their annealing processes for use in printed electronics.

2. EXPERIMENTAL SECTION

2.1. Nanoparticle Synthesis. Modified literature procedures were used to synthesize Silver nanoparticles.[25] We dissolved 6.5 mmol of $AgNO_3$ in 170 mL of isopropanol, to which we added 13 mmol of dodecane thiol dropwise while stirring. Immediately, 26 mmol of $NaBH_4$ was slowly added in 170 mL of isopropanol, and the solution turned a dark brown color. The reaction was allowed to stir for 5 min, after which ca. 300 mL of toluene was added followed by ca. 200 mL of water. The solution was transferred to a separatory funnel, and the aqueous phase was removed. The organic phase was washed five times with ca. 200 mL of water. The organic phase was isolated, and the solvent was removed under reduced pressure. The dry powder was suspended in ethanol and filtered using a Buchner funnel. It was subsequently washed with ethanol and acetone, allowed to dry, and collected. Size was determined using an FEI transmission electron microscope (TEM).

2.2. Thin Film Deposition and Sintering. To form films, 0.01 g of nanoparticles was suspended in 1 mL of toluene. The solution was dispensed through a 0.45 μm PTFE filter, onto one-quarter of a 4 in. oxidized Si wafer with 100 nm of thermal SiO_2. The substrate was immediately spun at 1000 rpm following dispensing and was allowed to spin for 45 s.

Annealing was accomplished by placing samples onto a hot plate already at the given temperature, and then dwelling at that temperature for the recorded amount of time. Air annealing was performed in the normal ambient of the room, and inert annealing was accomplished in a glovebox, in which the oxygen levels were always kept below 20 ppm. After the substrate had been heated for the prescribed amount of time, they were immediately removed and cooled to room temperature. For DSC/TGA analysis, argon was used for the inert atmosphere.

2.3. X-ray Diffraction and Scattering. High resolution X-ray diffraction data were taken on BL2-1 at the Stanford Synchrotron Radiation Laboratory (SSRL). Rocking curves were taken on BL2-1. Soller slits (1 milliradian) were used as diffracted beam collimators. GIXS data were taken at BL11-3 with an MAR345 area detector and an X-ray energy of 12.7 keV.

2.4. Transmission Electron Microscopy. All TEM micrographs were obtained from either an FEI G2 with LaB_6 filament or an FEI Tecnai G2 F20 X-TWIN. Images were made of thick films heated under the specified conditions and then sonicated in toluene. The toluene was then dispersed on supported grids for imaging.

3. RESULTS AND DISCUSSION

As discussed above, we study the formation of order in films formed from sintered nanoparticles through use of calorimetry and thermogravimetric analysis, X-ray diffraction and scattering, and transmission electron microscopy. First, to understand the temperature-related transitions from particles to films, we correlate disorder of the SAMs surrounding the particle, identified by DSC analysis, to the loss of the superlattice observed by X-ray scattering. Since the superlattice is a result of the ligand-controlled particle separation, the relationship between these two identifies the temperature-defined points at which particles begin to interact to form films.

Finally, to establish an overall mechanism of sintering, we use a combined study of ordering observed by X-ray diffraction and particle structure observed by transmission electron microscopy to investigate film formation through the interaction of particles; specifically, we use studies on the size and structure of the particles versus texture and ordering seen in films to investigate the relative importance of particle aggregation, ripening, and digestion.

3.1. Disappearance of the Superlattice. We begin by establishing by TGA the presence of the surfactant throughout the annealing process. We next establish the relationship between the loss of the superlattice and the state of the ligands surrounding the particles. The superlattice can be used as an indicator of the particulate nature of the system, since the superlattice order results from a well-defined particle−particle spacing dictated by the chemisorbed ligands. This allows for the identification of the onset of interparticle interactions when the superlattice disappears. Figure 1A shows TEM micrographs of the nanoparticles used in this experiment, and Figure 1B shows the XRD of these same particles.

Using the Scherrer equation,[26] we can determine the crystallite size of the particles as 3.1 nm, in excellent agreement with the TEM data seen in Figure 1A, showing that the particles are single crystal.

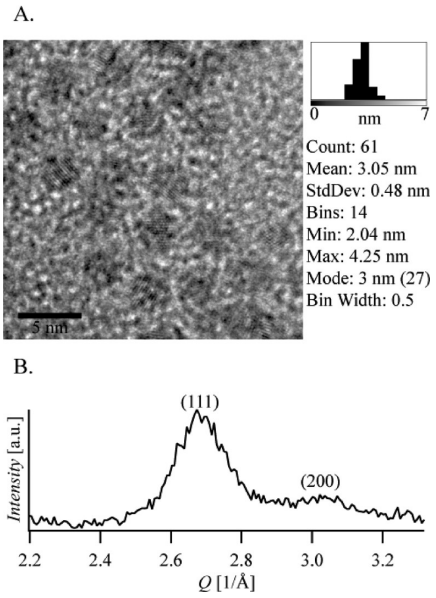

Figure 1. A) TEM micrograph of nanoparticles before sintering. Size distribution was obtained from measuring the diameter of particles on multiple micrographs of the same sample. B) XRD data for the same nanoparticles.

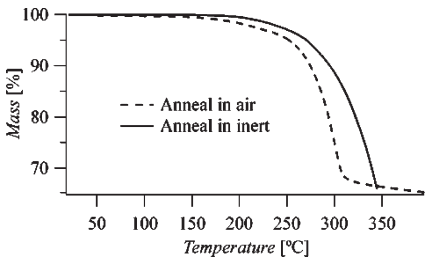

Figure 2. TGA data for the nanoparticles annealed in air and in an inert atmosphere — in this case argon.

The presence or absence of the surfactant in the film is crucially important because this affects the energy of the system. Figure 2 presents TGA data for the system as it is heated in both air and an inert environment - in this case argon.

Figure 2 shows that the surfactant remains in the film at 200 °C as there is less than 1% mass loss at 200 °C. Others have suggested in similar studies on gold thiol systems that some critical level of stabilizing ligand must be removed from the nanoparticles before sintering can occur.[16,17] In this study, on the sintering of silver particles, we show that this is not the case. Indeed, the films become fully conductive even in the presence of the surfactant.

Next we establish the temperature at which the surfactants surrounding the particles begin to disorder. Figure 3 A and D shows the thermal response of the system. The strong endothermic response seen in the calorimetric data at 132 °C for the air annealing (Figure 3A), and at 142 °C for the inert annealing (Figure 3D), correspond to the disordering, or melting, of the alkyl chains of the thiol SAMs that surround the particles.[27,28] Since particles cannot sinter while separated from each other by well-ordered thiols, this marks a necessary, though not sufficient, condition for sintering to occur.

Next we show the loss of the periodic ordering of the particles in the film as we anneal at temperatures above that where the

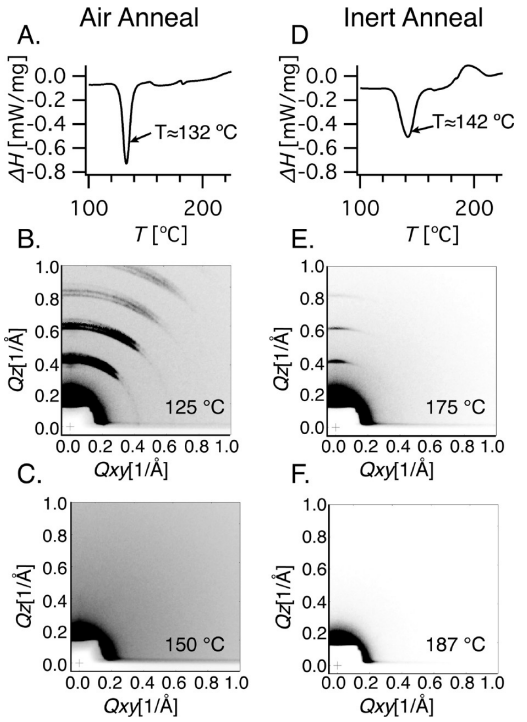

Figure 3. A) Calorimetric response of particles annealed in air and D) in Ar. B) XRD data for annealing at 125 °C in air, C) 150 °C in air, E) 175 °C in N_2, and F) and 187 °C in N_2. The dark areas near the origin (Qz = Qxy = 0) are scattering from the windows in the sample cell.

SAMs surrounding the particle disorder. Representative GIXS data are shown in Figure 3B, C, E, and F. As deposited, the particles pack in a regularly ordered superlattice,[28] as indicated by the low Q scattering peaks associated with interparticle spacing (Figure 3B). All X-ray data are taken on films after cooling to room temperature and are not performed in situ. Figure 3B and 3C display GIXS data for nanoparticles dispersed onto an amorphous SiO_2 substrate, isothermally heated in air below and above the endothermic transition at 132 °C. The low Q scattering associated with the interparticle spacing in the ordered superlattice disappears between 125 and 150 °C for samples heated in air, showing the loss of the superlattice. In the annealing performed in an inert environment, the superlattice persists to >175 °C (Figure 3E), well above the temperature at which the SAM disorders at 142 °C. Finally, between 175 and 187 °C (Figure 3F) we see the superlattice fully disappear. From this, we conclude that the disordering of the alkyl chain and the loss of the superlattice do not always occur at the same temperature and that the loss of the superlattice occurs at a higher temperature than the disordering of the surfactant.

3.2. Crystallite Growth and Texturing of Films. Next we show how the crystallite size and orientation vary as a function of annealing temperature and ambient. Diffraction is used to examine the onset of order within the resultant film, and microscopy is used to examine particle structure during film formation. Since the size, distribution, and structure of the ordering particles can be related to the mechanisms at play, i.e., aggregation, ripening, and digestion, we are able to use this methodology to provide insight into the overall mechanism of sintering in these systems. Once the superlattice disappears, crystallite growth begins. It is at this point that the SAM surrounding the particle

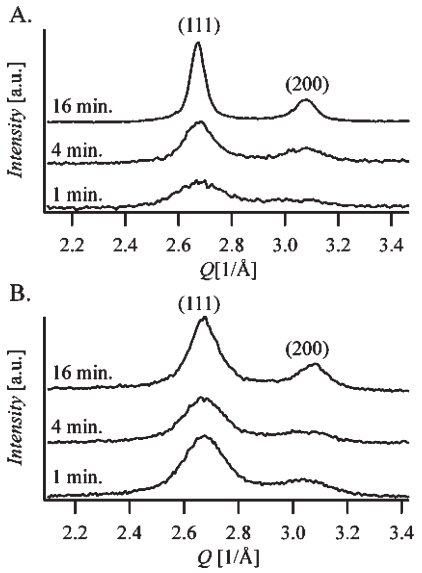

Figure 4. A) Diffraction data for samples annealed at 150 °C in air and B) 187 °C in N_2.

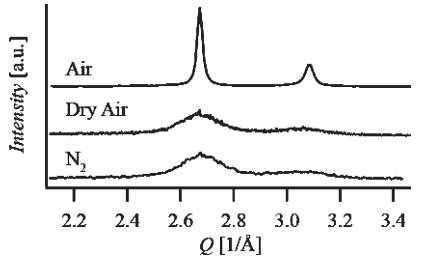

Figure 5. Diffraction data for samples annealed at 175 °C for 16 min in air, dry air, and nitrogen. (Signal multiplied by a factor of 30 for the annealing in dry air, and a factor of 10 for the annealing in nitrogen.)

disassociates from the surface of the particle and begins to act like a solvent in which the film grows. In air this occurs at 150 °C and in nitrogen at 187 °C. Figure 4 shows XRD data as a function of time for samples annealed at these temperatures.

The sharpening of the XRD peaks in Figure 4A and B is due to an increase in size of the silver crystallites, which can be quantified using the Scherrer equation. Crystallite growth occurs more rapidly in air than in nitrogen even though the nitrogen annealing is performed at a higher temperature. This is predominantly due to the moisture in the air and not the oxygen. This is demonstrated by Figure 5, which shows XRD data for particles heated at 175 °C for 16 min in air, dry air, and nitrogen.

Particles heated in dry air and nitrogen result in no crystallite growth at these conditions, in contrast to those heated in ambient lab air. This indicates that moisture is the dominant factor responsible for the differences between the annealing in air and inert environments. The detailed underlying reasons for this behavior are beyond the scope of this paper.

Figure 6 shows TEM micrographs for particles annealed in air. This provides evidence of crystallite growth proceeding by coalescence (Figure 6A) and of the formation of particles smaller than the initial particles (Figure 6B).

In Figure 6A we note the result of two particles coming together to form a single crystallite through coalescence.

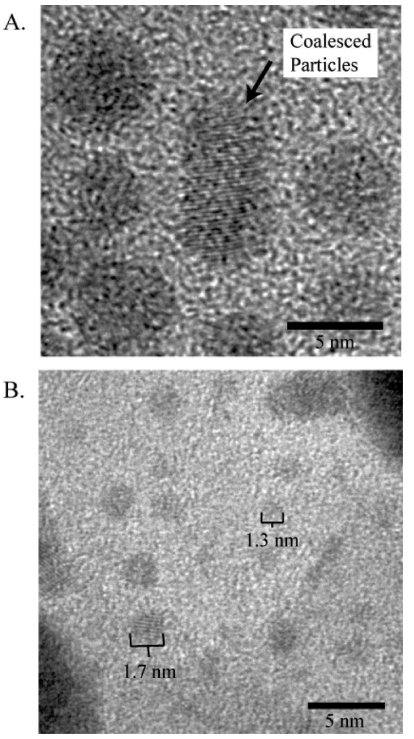

Figure 6. A) TEM micrograph of particle heated for 4 min at 150 °C in air and B) of particles heated for 16 min at 150 °C in air.

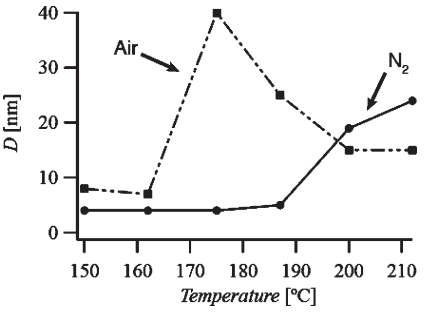

Figure 7. A) Summary of crystallite size derived from XRD data for films annealed in air and N_2.

In Figure 6B we see particles smaller than our initial particles of about 3 nm (Figure 1A). This indicates one or more mechanism besides coalescence at work in the system.

Figure 7 summarizes crystallite size information, derived from the XRD data using the Scherrer equation.

Crystallite size was determined on thin films dispersed onto SiO_2 substrates, heated at the desired temperature for 16 min. Films were rapidly heated to the desired temperature by placing them on a hot plate already at that temperature. We note that crystallite growth in both the air and nitrogen annealing processes occurs only after the loss of the superlattice, which, in turn, occurs only after the disordering of the thiols. Remarkably in air, crystallite size is smaller at 200 °C than at 175 °C. In nitrogen, crystallite size increases over the temperature range of the experiment, with the onset of crystallite growth retarded relative to the annealing performed in air, though with a larger crystallite size at 200 °C.

The other major difference in film morphology between air and inert annealing processes is the tendency of the films to

dx.doi.org/10.1021/cm202561u |*Chem. Mater.* 2011, 23, 4634–4640

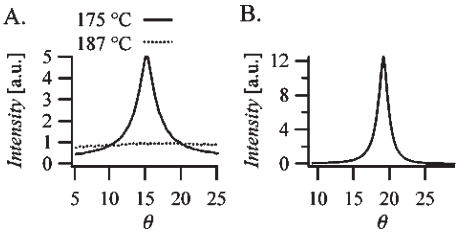

Figure 8. (111) rocking curves for samples annealed A) at 175 and 187 °C in air (signal for 187 °C multiplied by a factor of 5) and B) at 200 °C in N_2.

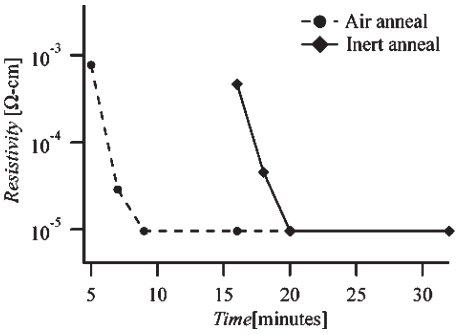

Figure 9. Resistivity of films annealed over time in air and inert atmospheres.

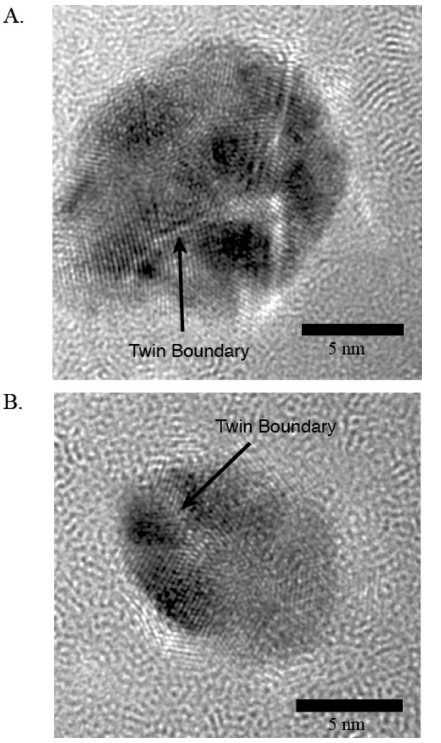

Figure 10. HREM micrographs of coalesced silver particles after heating at 200 °C for 15 s in A) air and B) N_2 with arrows showing examples of twin boundaries.

crystallographically texture. To probe this, rocking curves were collected. Here, the diffractometer is positioned at a Bragg peak, in this case the silver (111) peak, and the sample is then rotated about this condition. If the film is highly oriented, there is a sharp peak. Figure 8A and B shows rocking curves for particles annealed in air and nitrogen.

In air, only those samples annealed close to 175 °C are textured (Figure 8A). Samples annealed at lower temperatures consist of individual particles and thus are randomly oriented. Films annealed at 187 °C and above are not oriented, although they are sintered, as evidenced by electronic conductivity and adhesion to the substrate. We see that all the films annealed in nitrogen above 200 °C (Figure 8B) orient relative to the substrate; those annealed below 200 °C remain as individual particles and are thus untextured.

3.3. Mechanism of Sintering. Next we show that higher rates of aggregation in the particle system tends to lead to smaller crystallite sizes, less orientation, and greater twinning in the particles; this, likewise, results in films that tend to have smaller crystallite sizes and are not oriented. The relative rates of aggregation can be observed directly from the time it takes for films to become conductive. Figure 9 displays the resistivity of films heated at 200 °C in both air and inert.

Since conductivity is reached in the air anneal faster than in the inert anneal, the rate of aggregation is faster in air.

For annealing in both air and nitrogen, coalescence is important in the early stages of crystallite growth, when particles are still small. This can be seen from Figure 10, which shows particles heated for 15 s at 200 °C; the coalescence of multiple particles is visible from the formation of twin boundaries in the particles.

However, in later stages of growth, aggregation inhibits crystallite growth and the development of orientation. The resulting morphology of the particles and the film can be understood in terms of a competition between aggregation and ripening (independent of the ripening process). As already mentioned, Figure 9 shows that one of the effects of air is to increase the rate of aggregation. When the rate of aggregation is faster (air at 200 °C), both crystallite size (Figure 7) and crystal orientation (Figure 8) decline relative to the nitrogen annealed samples. Figure 11 shows this effect for nanoparticles annealed at 200 °C for 1 min in air and N_2.

Particles annealed in air typically display twinning and multiple crystallite directions (Figure 11 A-C). These twins persist in the ripening process and what results are particles with no preferential orientation. In contrast to this are the nitrogen annealed samples, in which the rate of aggregation is slower (Figure 9). Here crystallites grow larger (Figure 7), and films orient more strongly (Figure 8). Whether this ripening is due solely to aggregative growth or whether there is a component of Ostwald ripening is beyond the scope of this paper. Regardless, this slower rate of aggregation leads to particles that tend to be single crystal (Figure 11D and 11E) or with very few grain or twin boundaries (Figure 11F). This is further supported by Figure 12, which shows the population of particles with and without twin boundaries for particles heated in air and nitrogen.

Here, the particles examined were between 300 nm^2 and 600 nm^2 in size, to represent the later stages of growth. Particles heated in air show a strong tendency for multiple twin and grain boundaries compared to particles heated in nitrogen. Thus, we see when aggregation is faster, particles tend to have more twin boundaries, a higher degree of polycrystallinity, and to consist of smaller crystallites; in turn, the films that result from them also have smaller crystallites and tend to be unoriented.

3.4. Digestive Ripening. The final observed mechanism of particle formation is that of digestive ripening. In this process,

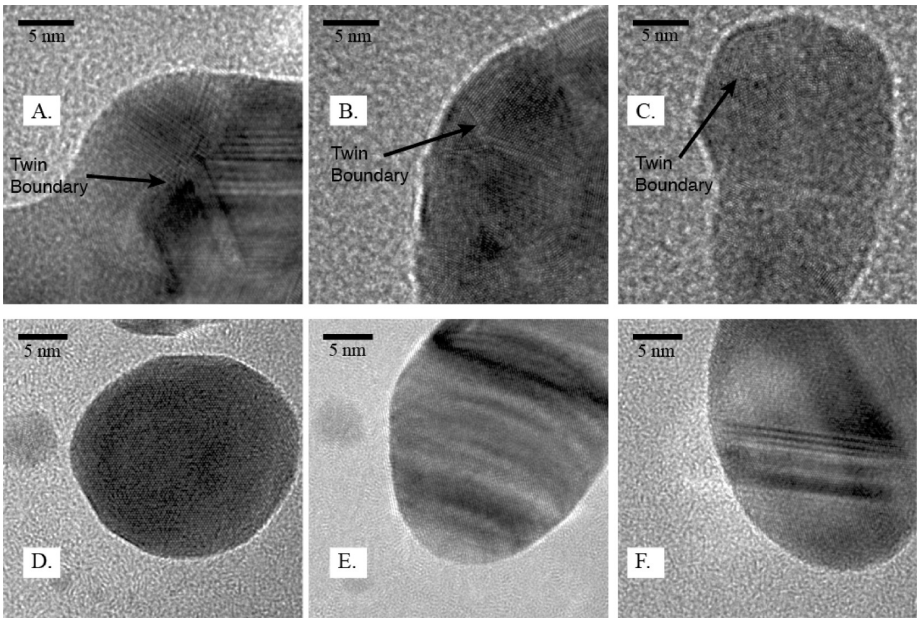

Figure 11. A-C) HREM micrographs of particles heated for 1 min in air at 200 °C with arrows showing examples of twin boundaries. D-F) HREM micrographs of particles heated for 1 min in N_2 at 200 °C.

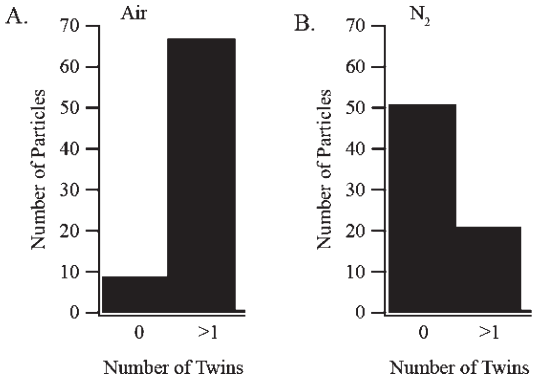

Figure 12. Distribution of particles with and without twins for anneals at 200 °C for 1 min in A) air and B) N_2.

larger particles are eroded and smaller particles are formed. This process is characterized by the formation of superlattice structures that result from the partially eroded larger particles.[21] We only observe this in the air annealed samples and see it at both 175 and 200 °C. We rule out the possibility that these superlattices are derived from the rapid aggregation of particles in the nanoparticle superlattice (e.g., Figure 3). We state this for two reasons: first, we observed the disappearance of this superlattice by small-angle X-ray scattering (Figure 3C and F); second, we do not observe these superlattice structures in our initial sampling of the films; they are only observed after longer time intervals. Figure 13 shows these superlattice structures.

The lattice spacing for the film heated at 175 °C is 6 nm, and for the one heated at 200 °C is 3 nm. Selected area diffraction (SAD) of the superlattice in Figure 13A, displayed in the inset, shows that the crystallites of the superlattice are oriented. This is taken at a sintering condition where we expect the film to be textured (Figure 9A, 175 °C, 16 min), showing that this superlattice is derived from the sintered film already oriented to the

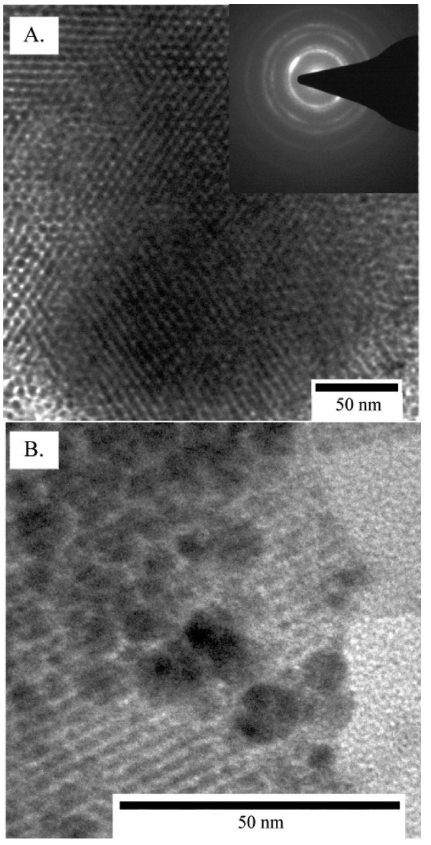

Figure 13. TEM micrographs of superlattice structures from samples heated at A) 175 °C for 16 min in air and B) 200 °C for 1 min in air.

substrate. The ultimate product of digestive ripening is a film of nanoparticles derived from either the erosion of larger particles or the film itself. This process, therefore, competes with aggregation

dx.doi.org/10.1021/cm202561u |*Chem. Mater.* 2011, 23, 4634–4640

and ripening, to break up the film. Since conductivity is eventually achieved, we can assume mechanisms contributing to film formation prevailed. However, it would not be surprising to find conditions where the rate at which conductivity was achieved was slowed by digestion.

4. CONCLUSION

The sintering of silver nanoparticles into films of high electrical conductivity can be achieved in the presence of the surfactant used to coat the particles. The surfactant separates the particles from each other, which form into a supperlattice. The surfactant prevents interaction between particles, and it is the disassociation of the surfactant from the particles that leads to the loss of the superlattice and gates the initial stages of sintering. We see in this silver thiol system that moisture changes the interaction of the surfactant with the particle, such that the onset of sintering occurs at a lower temperature and the rate of aggregation is increased. Furthermore, we see that the increased rate of aggregation brought about by the effects of moisture on the system increases the occurrence of twinning and polycrystallinity within the particles and reduces the crystallite size and orientation within the resultant film. We also notice the presence of digestive ripening, which can convert large particles back to smaller particles thus inhibiting the sintering process and, in extreme cases, possibly prevent sintering. This mechanism principally manifests itself in the air anneals and in the later stages of sintering.

The understanding we have gained on the sintering of metal nanoparticles into films is important for a variety of applications. First, as discussed previously, the use of nanoparticles as inks for printed electronics has become widespread, and a mechanistic understanding of sintering is critical to understanding and optimizing film formation in these systems. Further, because different crystal planes have different work functions, film texture will change the effective film work function. Similarly, in the formation of microelectronic mechanical systems (MEMS), such as cantilevers, the mechanical properties of the films are drastically affected by the orientation of the metal films[29] as well as the grain size. In catalytic applications, the catalytic activity of metallic particles is strongly affected by their diameter.[4] We have shown that by changing the annealing process, one can change both the texture and grain size and thus tune properties such as those mentioned above.

■ ASSOCIATED CONTENT

Supporting Information. X-ray diffraction pattern (XRD) of particles annealed in air and under inert conditions. This material is available free of charge via the Internet at http://pubs.acs.org.

■ AUTHOR INFORMATION

Corresponding Author
*E-mail: svolkman@eecs.berkeley.edu.

■ ACKNOWLEDGMENT

UC Discovery and Henkel Electronic Materials funded portions of this research. Portions of this research were carried out at the Stanford Synchrotron Radiation Lightsource, a national user facility operated by Stanford University on behalf of the U.S. Department of Energy, Office of Basic Energy Sciences. The authors would like to thank Trevor Ewers for helpful discussion.

■ REFERENCES

(1) Lai, S.; Guo, J.; Petrova, V.; Ramanath, G.; Allen, L. *Phys. Rev. Lett.* **1996**, *77*, 99–102.
(2) Buffat, P.; Borel, J.-P. *Phys. Rev. A* **1976**, *13*, 2287–2298.
(3) Ercolessi, F.; Andreoni, W.; Tosatti, E. *Phys. Rev. Lett.* **1991**, *66*, 911–914.
(4) Valden, M.; Lai, X.; Goodman, D. W. *Science* **1998**, *281*, 1647–1650.
(5) Kreibig, U.; Vollmer, M. *Optical Properties of Metal Clusters*, 1st ed.; Springer: 1995.
(6) Maier, S. A.; Brongersma, M. L.; Kik, P. G.; Meltzer, S.; Requicha, A. A. G.; Atwater, H. A. *Adv. Mater.* **2001**, *13*, 1501–1505.
(7) Kelly, K. L.; Coronado, E.; Zhao, L. L.; Schatz, G. C. *J. Phys. Chem. B* **2003**, *107*, 668–677.
(8) Sonnichsen, C.; Reinhard, B. M.; Liphardt, J.; Alivisatos, A. P. *Nat. Biotechnol.* **2005**, *23*, 741–745.
(9) Perelaer, B. J.; Laat, A. W. M.; de; Hendriks, C. E.; Schubert, U. S. *J. Mater. Chem.* **2008**, *18*, 3209–3215.
(10) Xue, F.; Liu, Z.; Su, Y.; Varahramyan, K. *Microelectron. Eng.* **2006**, *83*, 298–302.
(11) Wu, Y.; Li, Y.; Ong, B. S. *J. Am. Chem. Soc.* **2006**, *128*, 4202–4203.
(12) Schubert, G.; Huster, F.; Fath, P. *Sol. Energy Mater. Sol. Cells* **2006**, *90*, 3399–3406.
(13) Brabec, C. J.; Sariciftci, N. S.; Hummelen, J. C. *Adv. Funct. Mater.* **2001**, *11*, 15–26.
(14) Springer, J.; Poruba, A.; Mullerova, L.; Vanecek, M.; Kluth, O.; Rech, B. *J. Appl. Phys.* **2004**, *95*, 1427–1429.
(15) Huang, D.; Liao, F.; Molesa, S.; Redinger, D.; Subramanian, V. *J. Electrochem. Soc.* **2003**, *150*, G412–G417.
(16) Wu, Y.; Li, Y.; Liu, P.; Gardner, S.; Ong, B. S. *Chem. Mater.* **2006**, *18*, 4627–4632.
(17) Coutts, M. J.; Cortie, M. B.; Ford, M. J.; McDonagh, A. M. *J. Phys. Chem. C* **2009**, *113*, 1325–1328.
(18) Nanda, K. K.; Maisels, A.; Kruis, F. E.; Fissan, H.; Stappert, S. *Phys. Rev. Lett.* **2003**, *91*, 106102.
(19) Penn, R. L.; Banfield, J. F. *Science* **1998**, *281*, 969–971.
(20) Huang, F.; Zhang, H.; Banfield, J. F. *Nano Lett.* **2003**, *3*, 373–378.
(21) José-Yacamán, M.; Gutierrez-Wing, C.; Miki, M.; Yang, D.-Q.; Piyakis, K. N.; Sacher, E. *J. Phys. Chem. B* **2005**, *109*, 9703–9711.
(22) Chen, Y.; Palmer, R. E.; Wilcoxon, J. P. *Langmuir* **2006**, *22*, 2851–2855.
(23) Lin, X. M.; Sorensen, C. M.; Klabunde, K. J. *J. Nanopart. Res.* **2000**, *2*, 157–164.
(24) Prasad, B. L. V.; Stoeva, S. I.; Sorensen, C. M.; Klabunde, K. J. *Chem. Mater.* **2003**, *15*, 935–942.
(25) Murthy, S.; Bigioni, T. P.; Wang, Z. L.; Khoury, J. T.; Whetten, R. L. *Mater. Lett.* **1997**, *30*, 321–325.
(26) Scherrer, P. *Nachr. Gesellschafts Wissenschaftlich Göttingen* **1918**, *2*, 98–100.
(27) Carotenuto, G.; Marletta, G.; Nicolais, L. *J. Mater. Sci. Lett.* **2001**, *20*, 663–665.
(28) Sandhyarani, N.; Resmi, M. R.; Unnikrishnan, R.; Vidyasagar, K.; Ma, S.; Antony, M. P.; Selvam, G. P.; Visalakshi, V.; Chandrakumar, N.; Pandian, K.; Tao, Y.-T.; Pradeep, T. *Chem. Mater.* **2000**, *12*, 104–113.
(29) Faurie, D.; Renault, P.-O.; Le Bourhis, E.; Goudeau, P. *Acta Mater.* **2006**, *54*, 4503–4513.